Corrosion Science 158 (2019) 108073

Contents lists available at ScienceDirect

Corrosion Science

journal homepage: www.elsevier.com/locate/corsci

The kinetics and mechanism of filiform corrosion occurring on zinc-aluminium-magnesium coated steel

N. Wint*, D. Eaves, E. Michailidou, A. Bennett, J.R. Searle, G. Williams, H.N. McMurray

Materials Research Centre, College of Engineering, Swansea University, Bay Campus, Fabian Way, Crymlyn Burrow, Swansea, SA1 8EN, UK

ARTICLE INFO

Keywords:
A. Steel
A. Magnesium
A. Metal coatings
C. Atmospheric Corrosion
C. Polymer coatings

ABSTRACT

This paper describes a systematic study into the initiation and propagation of filiform corrosion (FFC) on industrially important Zinc-Aluminium-Magnesium (ZAM) alloy coatings for steels. An artificial scribe defect is created in model organic coatings applied to ZAM. Corrosion is initiated using HCl, NaCl, $FeCl_2$ and acetic acid. Only acetic acid is able to reproducibly initiate FFC. The FFC (area) rate is shown to be proportional to the amount of acetic acid introduced. The FFC mechanism is explained in terms of the relative susceptibility of alloy phases to anodic dissolution, determined using scanning electron microscopy and scanning Kelvin probe force microscopy.

1. Introduction

In recent years there has been a great increase in the use of magnesium as an alloying element in galvanized coatings applied to steel surfaces to provide cathodic protection. Both hot dip [1–11] and physical vapour deposition (PVD) [12,13] processes have been used to apply ZAM and zinc-magnesium coatings to steel used for building and automotive purposes. Very significant quantities of organically overcoated zinc-aluminium-magnesium (ZAM) hot dip galvanised steel are now in service in both the architectural and automotive sectors. In this paper we draw attention to an important mode of corrosion driven organic coating failure which does not typically occur on conventional galvanized steel but which can occur on ZAM. This mode of corrosion-driven failure is filiform corrosion (FFC) initiated by a carboxylic acid (acetic acid).

For bare galvanized steel (without an organic overcoat) the kinetics and mechanism of zinc alloy corrosion has been widely investigated in a range of environments [1–30]. It has thus been shown that corrosion-driven mass loss from ZAM coated steel can be approximately two to three times lower than that from Zn coated steel (of comparative thickness) after 4 years of exposure in a variety of locations worldwide [22]. The addition of magnesium and aluminium to zinc results in the formation of a range of new phases of varying composition. The Al containing phases are generally considered stable in comparison to the more active zinc matrix [1,7,18,23]. Conversely, $MgZn_2$ and $MgZn_{11}$ intermetallics (IMs) have been found to undergo preferential anodic dissolution [1,7,18,22,23].

Magnesium is thought to improve corrosion resistance principally through the chemical modification of corrosion products [24], and increased corrosion product adhesion [25]. Anodic dissolution of Mg-rich phases releases Mg^{2+} ions which can react with OH^- (produced at the cathode) to form magnesium hydroxide ($Mg(OH)_2$). Replacing zinc (hydr)oxide with $Mg(OH)_2$ at the ZAM surface [4,11,21], is thought to reduce rates of the cathodic oxygen reduction reaction (ORR) [7,11]. The presence of $Mg(OH)_2$ can also 'buffer' surface pH to mildly alkaline values at which protective hydrozincite ($Zn_5(CO_3)_2(OH)_6$) and simonkolleite ($Zn_5(OH)_8Cl_2{\bullet}(H_2O)$) become stable [1,6]. This stabilization is believed to prevent their transformation into more soluble zinc compounds [26,27]. At similar values of pH, aluminium is predicted to become anodically active. Aluminates, produced through anodic dissolution of aluminium rich phases, can then react with Mg^{2+} to form protective layered double hydroxides (LDH) [1,6,15,22].

The corrosion of organic coated ZAM has been less widely studied. However, organic (over)coats are frequently applied to ZAM coated steel and corrosion-driven organic coating failure, is therefore a matter of concern [11,28–30]. Corrosion-driven organic coating failure processes, such as cathodic delamination and filiform corrosion (FFC), become initiated when an aggressive electrolyte comes into contact with the metal substrate. This typically occurs at penetrative defects in the organic coating, such as at cut-edges, fixing holes, scribes and scratches. The corrosion phenomena involved are atmospheric, occurring at high relative humidity but in the absence of bulk electrolyte immersion.

During cathodic delamination it is the cathodic ORR which is

* Corresponding author.
E-mail address: n.wint@swansea.ac.uk (N. Wint).

https://doi.org/10.1016/j.corsci.2019.06.028
Received 11 May 2019; Received in revised form 23 June 2019; Accepted 29 June 2019
Available online 09 July 2019

responsible for disbondment of the organic coating from the metal substrate. Anodic metal dissolution, occurring in the defect region, is coupled to a cathodic delamination front via a thin (< 5 μm) gel-like layer of electrolyte which ingresses beneath the coating [31–33]. Cathodic disbondment requires an aqueous electrolyte to be present at the coating defect which contains group (I) cations (such as Na^+). Only group (I) cations possess the solubility at high pH necessary to support the strongly alkaline catholyte which forms at the delamination front [31–33]. Corrosion-driven cathodic delamination of organic coatings has been widely reported to occur on zinc [34–39]. Conversely, organic coated $MgZn_2$ (one of the predominant phases present within ZAM alloys) [3,18,40,41] has been shown to resist cathodic delamination [11,28–30]. This finding has been (primarily) attributed to an inversion of the normal difference in electrochemical potential observed between the anodically active defect and the intact organic coated $MgZn_2$ surface [28–30].

FFC has been shown to occur on a variety of organically coated metals [42] including iron and steel [43–46], aluminium alloys [47–51] and magnesium [52], and can be initiated by very small quantities of aggressive electrolyte. It has been widely studied and is the subject of several reviews [31,42,43]. Examples of electrolytes which have been shown to initiate FFC include $FeCl_2$, [45,53], HCl, [50,54–56], NaCl [47,53], and acetic acid (CH_3COOH), (which will be denoted as HAc from this point forward) [57–65]. In FFC aqueous electrolyte only exists in the form of a small droplet at the head of each individual filament, maintained by the hygroscopicity of the salts therein. The FFC mechanism, as it occurs on iron and aluminium alloys, is generally believed to involve anodic metal dissolution occurring at, or near, the front of the head droplet [31,42,43]. The ORR occurs primarily towards the rear of the head droplet, where alkalization precipitates water-insoluble metal oxides and hydroxides. Facile O_2 diffusion along the porous, corrosion product tail then drives the filament head forward through differential aeration [31,42–47]. The same authors who demonstrated the ability of organic coated $MgZn_2$ to resist cathodic delamination [11,28–30] pointed out that the observed inversion of normal potential difference between the anodically active defect and the intact organic coated $MgZn_2$ surface increased the probability that organic coating delamination might occur through anodic undercutting, such as that which occurs during FFC [11,28].

Here we present a detailed study of FFC as it occurs on hot-dipped ZAM coated steel (in which the ZAM layer contains 1.5 wt% Al and 1.5 wt% Mg) overcoated with polyvinyl butyral co-vinyl alcohol-co-vinyl acetate (PVB). The kinetics and mechanism of FFC are studied systematically by initiating corrosion via the application of small, controlled, quantities of different aqueous corrosive electrolytes to a penetrative defect in the PVB coating, followed by incubation at a controlled relative humidity. The electrolytes used ($FeCl_2$, NaCl, HCl and HAc) have all previously been shown to initiate FFC on organically coated iron and aluminium [43–56]. However, only HAc is shown to rapidly and reproducibly initiate FFC on ZAM. HAc is emitted in the course of many technological and biological processes [57]. It has been identified as one of the most ubiquitous environmental initiators of atmospheric corrosion on materials exposed to indoor environments [57–65] and analysis of the corrosion product formed on iron, copper, nickel, and zinc, stored under these conditions, has revealed metal-carboxylates, such as metal-acetates, as major components [62]. Filamentary atmospheric corrosion has previously been reported on uncoated zinc in the presence of carboxylic acids including HAc [63], propionic acid [61] and acetaldehyde [59].

The principal aim of the current paper is to systematically describe the kinetics and mechanism of HAc initiated FFC, as it occurs on organic coated ZAM. In so doing the rate of FFC propagation is determined as a function of the quantity of HAc used during initiation. A combination of scanning Kelvin probe force microscopy (SKPFM) and SEM/EDS, of the uncoated ZAM surface, is used to predict which microstructural phases are likely to form the anodes and cathodes in any galvanic cell which might form. These predications are tested by observing differential rates of anodic phase dissolution under free corrosion conditions. The mechanism of FFC propagation on ZAM is then explained in terms of selective phase dissolution and the role of the steel substrate. Additional mechanistic insight is provided by the use of in-situ scanning Kelvin probe (SKP) measurements, which show electrochemical potential relationships occurring within the actively propagating FFC localized corrosion cell.

2. Materials and methods

2.1. Materials

Zn-1.5 wt. % Al- 1.5 wt. % Mg coated steel was supplied by Tata Steel and consisted of 0.7 mm gauge mild steel coated with a 10 μm thick (140 $g.m^{-2}$) ZAM layer on each side. 5 cm × 5 cm sized coupons were cut from a larger sheet. Coupons were cleaned using an aqueous slurry of 5 μm polishing alumina and rinsed with distilled water, then degreased in hexane and allowed to dry in air. All the solvents and reagents used were of analytical grade and provided by the Sigma-Aldrich Chemical Company.

2.2. Methods

2.2.1. Materials characterisation

SEM images of the original (uncorroded) ZAM microstructure and the post-corrosion surface were obtained using a Hitachi TM3000 SEM with integrated Quantax 70 EDX Analyser. Prior to SEM corroded samples were ultra-sonicated in a non-polar hydrocarbon (hexane) for 10 minutes. Both the PVB organic coating, and any loose corrosion product present, were thus mechanically removed from corroded samples via a cavitation effect.

Secondary ion mass spectroscopy (SIMS) analysis of the corroded surface was carried out using a Millbrook Instruments MC300(Mk II) Chemical Microscope fitted with a Gallium ion source. The lateral resolution was 10 μm and the mass resolution was ± 0.1 Da. Prior to SIMS analysis the PVB film was removed by mechanical peeling whilst the corrosion product remained substantially in place.

2.2.2. Atomic force and scanning Kelvin probe force microscopy

Atomic Force Microscopy (AFM) and Scanning Kelvin probe force microscopy (SKPFM) were used to determine the topography and Volta potential difference existing between phases present within the original (uncorroded) ZAM microstructure. Coupons were lightly polished using 1 μm diamond polishing paste before rinsing with ethanol and being left to air dry. A JPK NanoWizard3 atomic-force microscope (AFM) with scanning Kelvin probe (SKP) equipped with a FM-50 Pointprobe® tip, was used to perform measurements in alternating current (AC) tapping mode. The SKP scanning was performed at 20 nm above the surface at 20 μm/s in air at approximately 50% relative humidity.

2.2.3. Cathodic delamination and anodic undercutting

The susceptibility of ZAM coatings to cathodic driven coating disbondment and anodic undercutting on contact with aqueous NaCl was investigated using 'Stratmann' [32–33] type corrosion cells. Insulating tape was applied to 2 parallel edges of the coupons and acted as a height guide for the 15% w/w ethanolic solution of polyvinyl butyral-co-vinyl alcohol-co-vinyl acetate (molecular weight 70, 000–100, 000) which was applied by bar casting before being allowed to dry in air [34,66]. This procedure gave a dry PVB film thickness of 30 μm, as measured using a micrometer screw gauge. Once the coating had dried it was partially peeled back to expose a small area of bare metal which served as an artificial defect. A clear adhesive tape/PVB barrier was formed between the intact polymer coated metal surface and the metal surface and the defect. Beads of non-corrosive silicone rubber were applied to the remaining edges in such a way that a reservoir was

formed. A 1 cm^3 aliquot of 0.86 $mol.dm^{-3}$ aqueous NaCl was then introduced into the defect reservoir to initiate coating delamination. Two types of sample were produced. In the first variant the ZAM coating within the defect region remained intact. In the second variant the ZAM was removed in the defect region to expose the steel substrate with the aim of initiating anodic undercutting. The ZAM coating in the defect region was removed using 2 mol dm^{-3} HCl prior to PVB coating. A relative humidity (RH) of 95% was maintained in the experimental chamber using open reservoirs of 0.86 $mol.dm^{-3}$ NaCl. The experimental temperature was 25 °C.

Filiform Corrosion; Two parallel strips of insulating tape were applied to coupons upon which PVB was bar-cast before being allowed to dry in air [45,50–54]. PVB coatings of 30 µm thickness were prepared on ZAM as before. Linear scribed penetrative coating defects of 10 mm length were then created using a scalpel blade. These defects were either scribed to the ZAM surface (ie. through the PVB layer only) or to the steel surface (ie. through both the PVB and ZAM layers). Aliquots (2 µL) of aqueous solution comprising various concentrations of either $FeCl_2$ (pH ~ 5), NaCl (pH ~ 5), HCl (pH ~ -0.3), or HAc (pH ~ 2) were applied to each defect using a micro-syringe. Following corrosion initiation, coupons were placed in an experimental chamber as before. A relative humidity (RH) of 93% was maintained using reservoirs of saturated $Na_2SO_410H_2O$ [45,50–54] and the temperature was 25 °C. Chamber air was refreshed weekly and digital optical images of the sample surface taken using a Canon EOS camera. The length of individual FFC filaments and FFC corroded area were determined by taking measurements from the digital images obtained using Sigma Scan Pro 5 image analysis software. The image analysis software was calibrated by specifying a pre-measured distance between two points and inputting the real distance. Each FFC experiment was repeated four times. Filiform measurements were taken from four individual scribes (2 samples each with 2 scribes) for each concentration of each electrolyte.

2.2.4. Scanning Kelvin probe

Potentiometric measurements were obtained under atmospheric conditions using SKP instrumentation described in detail elsewhere [66,67]. The reference probe consisted of a 125 µm diameter gold wire which was vibrated normal to the sample surface at a vibration frequency of 280 Hz. The peak to peak amplitude was 40 µm. SKP calibration was carried out using Ag/Ag^+, Cu/Cu^{2+}, Fe/Fe^{2+} and Zn/Zn^{2+} couples following a procedure established previously [66]. In the case of cathodic delamination studies the SKP reference probe was moved over the surface along a 12 mm line up to the boundary of the defect and scans took place at regular intervals. For FFC studies a 12 mm x 8 mm area was scanned continuously. In both cases, scans were recorded as a numeric grid on the SKP control computer. Open reservoirs of the appropriate reference solution (0.86 $mol.dm^{-3}$ NaCl for cathodic delamination and saturated $Na_2SO_410H_2O$ for FFC) were placed at the bottom of the SKP environment chamber to ensure that humidity was kept constant.

3. Results

3.1. Materials characterisation

An SEM image of the ZAM microstructure is shown in Fig. 1. The alloy coating consists of ~15–25 µm sized zinc dendrites (~30% surface area) within a coarse binary eutectic phase (~30% surface area) and a finer ternary eutectic (~40% surface area). The binary eutectic consists of zinc and $MgZn_2$ lamellae and exhibits a mean average lamella spacing of ~1 µm. The ternary eutectic consists of zinc, a zinc rich aluminium phase and $MgZn_2$ and the mean lamella spacing is ~400 nm [3,10].

Fig. 2a shows the topography of an area of the diamond polished ZAM alloy, as determined using AFM. The primary zinc dendrites

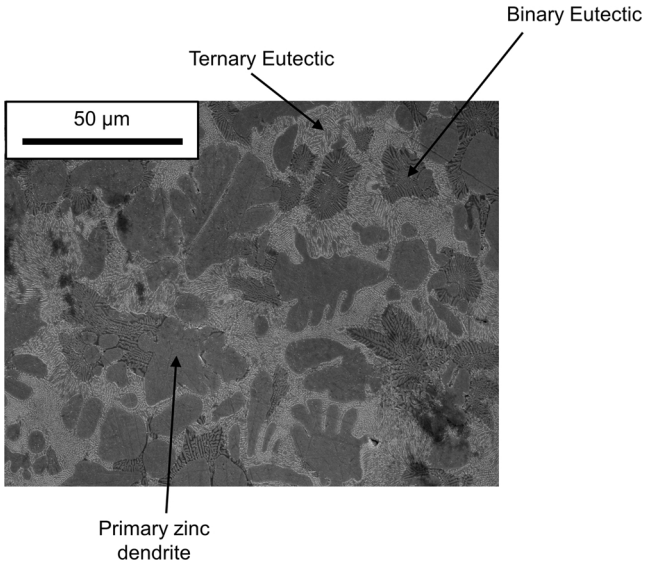

Fig. 1. SEM image of ZAM coating surface.

appear slightly raised compared to the eutectic phases. Fig. 2b and c show AFM topography and SKPFM Volta potential maps obtained from the inset area in Fig. 2a, respectively. Please note, the potential values shown in Fig. 2c have all been rebased such that highest potential is set to zero. The patterns of Volta potential difference seen in Fig. 2c correlate well with the topographical features (Fig. 2b). It therefore seems reasonable to propose that the observed Volta potential variations can be ascribed to local differences in surface composition. The Volta potentials associated with the primary zinc phase are similar to those of the zinc lamellae present within the binary and ternary eutectic. Lower potential values are observed for the $MgZn_2$ lamellae of the eutectic phases. The apparent Volta potential difference (contact potential) existing between the $MgZn_2$ lamellae and primary zinc is approximately 0.24 V. However, it must always be borne in mind that factors such as electrostatic charge spreading, tip dihedral capacitance and cantilever-sample capacitance all contribute towards the finite lateral resolution of the SKPFM and tend to reduce potential contrast [68–70]. The observed Volta potential differences should therefore be considered in terms of relative nobility as opposed to quantitatively. Nevertheless, given the approximately linear relationship typically observed between Volta (contact) potential and electrochemical potential [32,71], the Volta potential distributions in Fig. 2 suggest that the $MgZn_2$ lamellae will form the anode in any galvanic couple with primary zinc.

3.2. Attempts to produce cathodic delamination and anodic undercutting

When the steel substrate was not exposed in the Stratmann cell defect, neither cathodic disbondment (nor any other form of significant PVB coating disbondment) were observed to occur over a 6 month period, during which time the defect was in contact with 0.86 $mol.dm^{-3}$ aqueous NaCl. The ability of $MgZn_2$ (one of the predominant phases present within ZAM alloys) [3,18,40,41], to resist cathodic delamination, has been demonstrated previously [11,28–30]. The same authors who reported this finding also proposed that there was an increased probability that organic coating delamination from $MgZn_2$ might occur through anodic undercutting [11,28]. In an attempt to test this hypothesis, the ZAM coating was removed from the defect area prior to the introduction of 0.86 $mol.dm^{-3}$ aqueous NaCl. Under these circumstances cathodic coating delamination was once again not observed over a six month period. However, visible anodic dissolution of the ZAM coating at the defect edge and undercutting of the PVB coating was observed.

Fig. 3a shows a ZAM Stratmann cell in the case that the steel

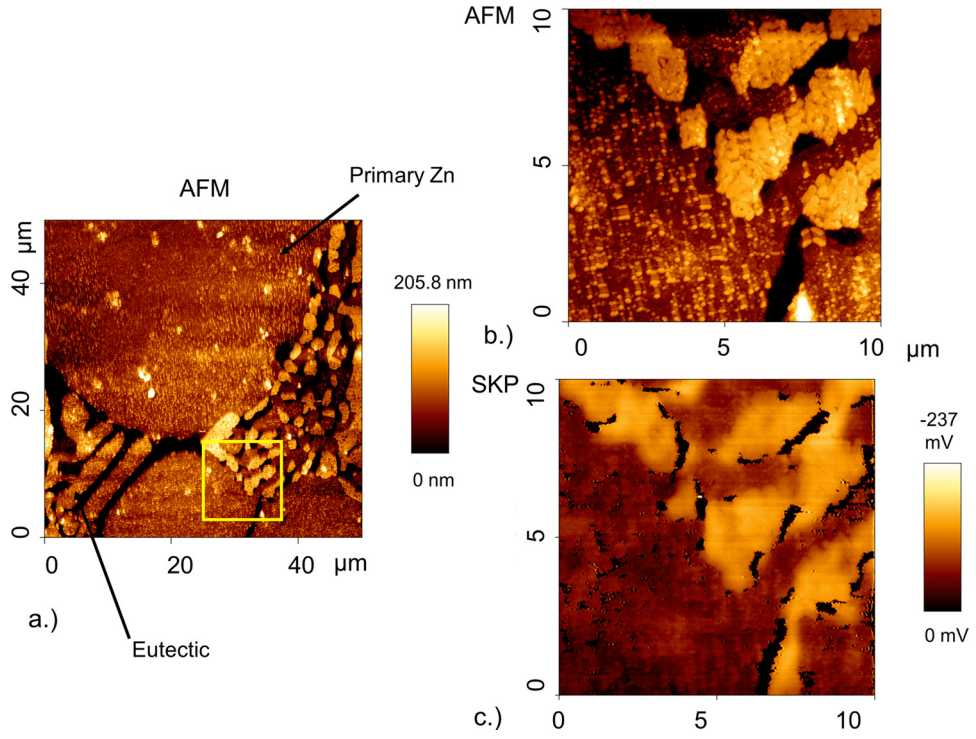

Fig. 2. a.) The topography of an area of the polished ZAM alloy, as determined using AFM, b.) the AFM topography and c.) SKPFM Volta potential map obtained from the inset area in a.).

substrate (within the defect area) is exposed. Red rust appears within the defect within 30 minutes of 0.86 mol dm^{-3} introduction. After 1 month visible anodic dissolution occurs at the defect edge and the propagation of FFC can be observed. After 3 months the length of an individual filament is ~1 cm. Fig. 3b shows photograph of the defect/intact coating interface in which the region of anodic undercutting is indicated with an arrow. Fig. 3b also shows the SKP derived distribution of E_{corr} values over the rectangular area indicated (with a red dashed line) in the photograph. Individual filament heads are seen as ~0.2 mm diameter areas of low potential (dark), and the tails as ~0.2 mm wide tracks of high potential (light). These potential distributions are qualitatively similar to potential distributions previously reported over FFC filaments actively propagating on aluminium alloys [47–51,54], and iron [43–46,53]. As such they help to confirm that the phenomenon observed is (similar to) conventional FFC. The background (non FFC filament) potential is a constant at ~-0.3 V vs SHE.

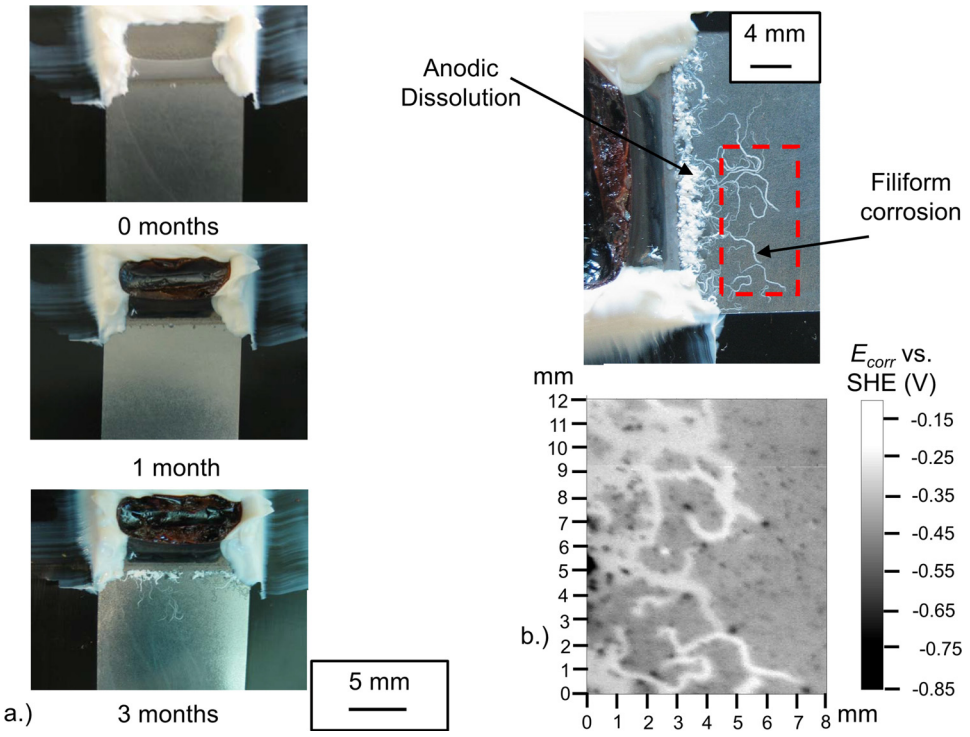

Fig. 3. Photograph of a ZAM coated steel Stratmann cell for which the coating has been removed within the defect region a.) at various times following introduction of 0.86 mol.dm^{-3} NaCl to artificial coating defect. b.) SKP derived distribution of E_{corr} in the rectangular area indicated in the photograph of the sample surface near the defect/intact coating interface.

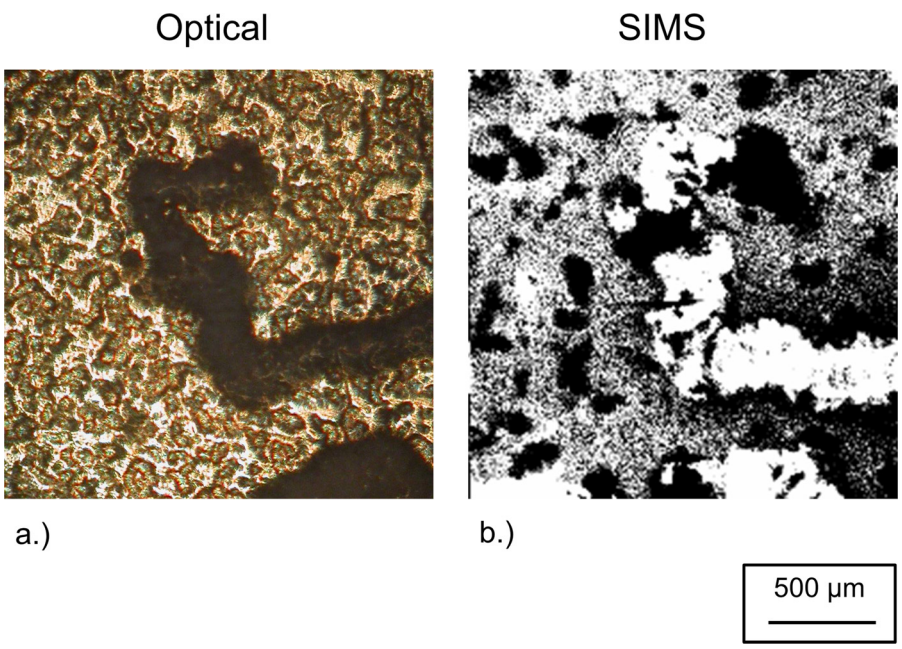

Fig. 4. An a.) optical and b.) secondary mass ion spectroscopy image of a typical FFC head and corrosion product tail propagating on ZAM following introduction of 0.86 mol.dm^{-3} NaCl to artificial coating defect.

This is similar to values previously reported for intact PVB coated zinc [34,36] and supports the notion that cathodic disbondment does not occur to any measurable extent on the PVB coated ZAM used in our experiments.

At the end of the experimental period the PVB coating was removed and an individual FFC filament was imaged using SIMS. Fig. 4a shows at secondary electron image of the filament and Fig. 4b shows the corresponding chlorine elemental map. Fig. 4b shows that the entire filament tail is abundant in Cl^- ions whereas minimal levels are detected within the FFC head.

3.3. Filiform corrosion study

Having serendipitously discovered the susceptibility of ZAM alloy coatings to FFC, a systematic study was undertaken with the aim of determining a methodology by which FFC could be initiated quickly and reproducibly on PVB coated ZAM. To this end, four aqueous electrolytes ($FeCl_2$, HCl, NaCl, HAc), which have previously been shown to initiate FFC on a range of metal substrates, were systematically investigated. In so doing 2 µL aliquots of electrolyte at concentrations ranging between 0.5 and 2 mol.dm^{-3} were injected into the scribed coating defect. When this was done none of the chloride based electrolytes were found to have initiated FFC at any of the experimental concentrations. Fig. 5 shows representative optical images of PVB coated ZAM samples taken 5 weeks after injection of 2 mol.dm^{-3} a.) $FeCl_2$, b.) HCl and c.) NaCl into a coating scribe which penetrated to the ZAM surface. In the case of $FeCl_2$ a brown-red rust layer can be seen along the defect but coating delamination is not observed. For HCl electrolytes a blister-like region of PVB coating delamination is shown. Dark localized attack is observed when using NaCl as an initiator but only limited disbondment of the coating occurs.

In contrast to the above, the HAc electrolyte was found to rapidly and reproducibly induce FFC at all the experimental concentrations. Fig. 6 shows the propagation of FFC on PVB coated ZAM over a 70 day time period. Two scribe defects have been made on the sample. The top scribe penetrates through both the PVB and ZAM coating to the steel substrate. The bottom scribe only penetrates to the ZAM coating. The number and width of FFC filaments is significantly greater in the case that the steel is exposed. Henceforward, all the results shown will be derived from samples in which the scribe penetrates down to the steel substrate. Fig. 7 shows an example of the optical images obtained for FFC propagating on ZAM over a 5-week period following initiation using 2 µL of 1.5 mol.dm^{-3} HAc. The FFC filaments appear white against the dark substrate. After 1 week, limited coating delamination is observed along the defect and FFC filaments extend perpendicular to the direction of the scribe. As time progresses more filaments continue to propagate away from the defect. There is no indication that the direction of this propagation is determined by factors such as substrate rolling or polishing direction and after 5 weeks some of the filaments have grown > 10 mm long.

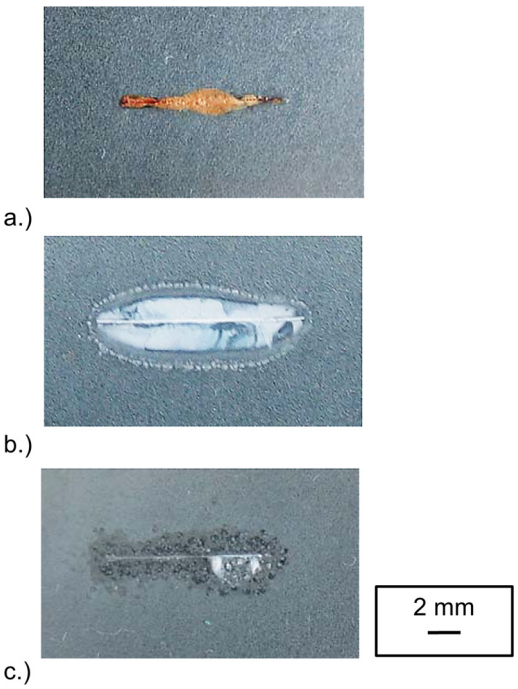

Fig. 5. Optical images of PVB coated ZAM samples taken 5 weeks after injection of 2 µL of 2 mol.dm^{-3} a.) $FeCl_2$, b.) HCl and c.) NaCl.

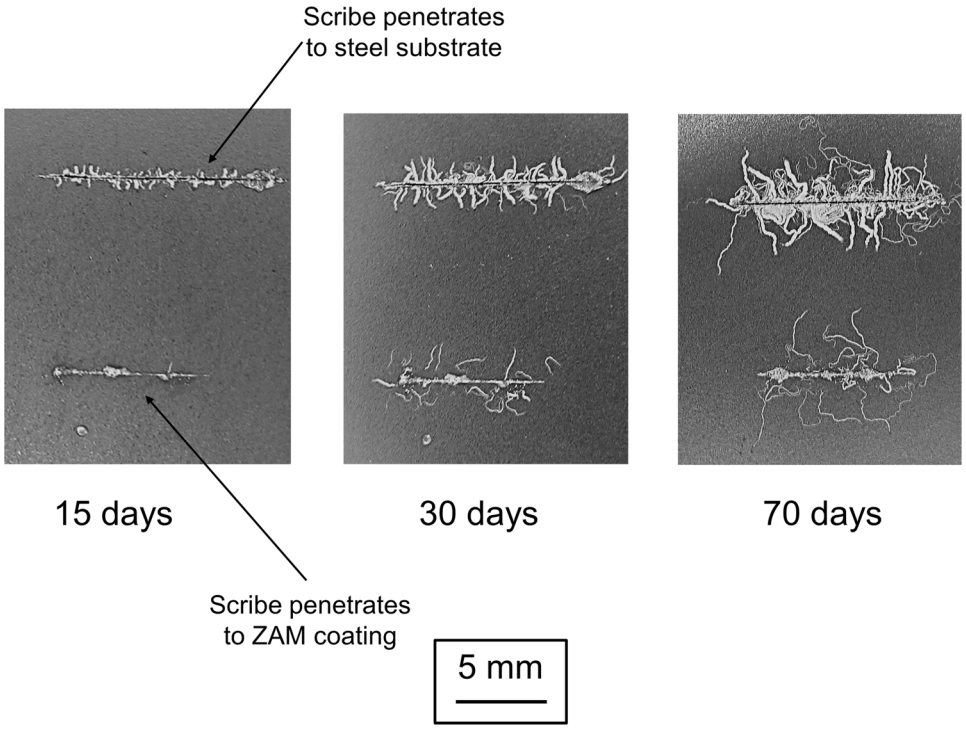

Fig. 6. Optical images of FFC propagating on ZAM over a 70 day period. FFC has been initiated by injecting 2 µL of 1.5 mol.dm^{-3} HAc to a scribe defect which penetrates to either the steel substrate or the ZAM coating.

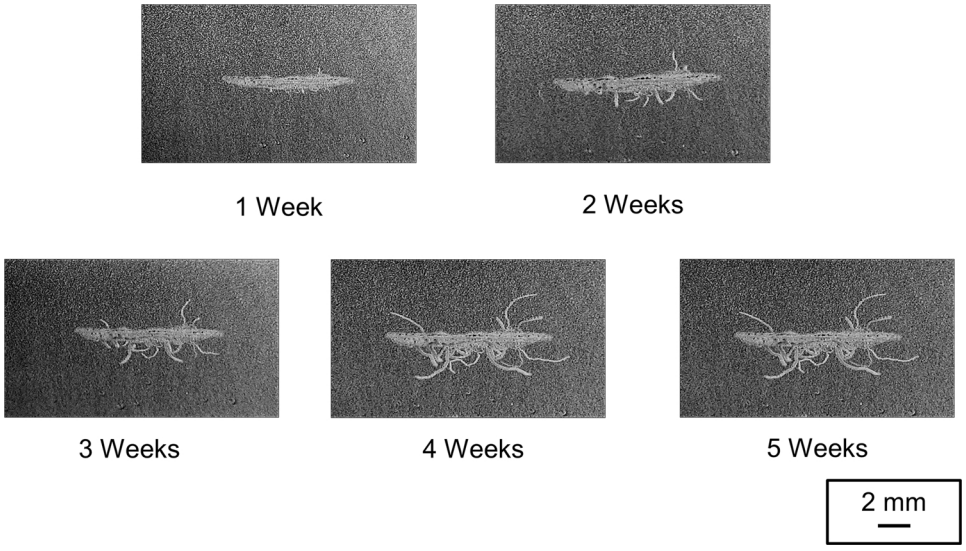

Fig. 7. Optical images of FFC propagating on ZAM over a 5-week period. FFC has been initiated by injecting 2 µL of 1.5 mol.dm^{-3} HAc to a scribe defect which penetrates to the steel substrate.

Table 1
Average length of FFC observed on ZAM after various periods of times following initiation using a range of HAc concentrations.

Time (weeks)	Length (mm)			
	0.5 mol.dm^{-3}	1.0 mol.dm^{-3}	1.5 mol.dm^{-3}	2 mol.dm^{-3}
0	0	0	0	0
1	0.25	0.56 ± 0.63	0.94 ± 0.25	1.31 ± 0.48
2	0.38 ± 0.5	1.31 ± 0.95	2.13 ± 0.87	2.56 ± 1.18
3	1.50 ± 1	2.5 ± 1.29	3.44 ± 1.44	4.19 ± 2.66
4	2.25 ± 1	3.44 ± 1.65	4.69 ± 2.53	5.25 ± 3.08
5	3.13 ± 1.5	4.69 ± 2.66	6.19 ± 3.59	6.94 ± 4.25

Similar images were acquired for each of the experimental concentrations of HAc and the FFC filament number and filament length data thus obtained is summarized in Table 1. Table 1 shows that an increase in HAc concentration has the effect of increasing the number of filaments observed from 1 for 0.5 mol.dm^{-3} HAc to 20 at concentrations of 2 mol.dm^{-3}. This trend is illustrated by Fig. 8 which shows the appearance of ZAM samples 5 weeks after initiation of FFC using varying HAc concentrations.

As a first approach, FFC propagation kinetics were estimated by measuring the time dependent length of individual filaments. The time dependent mean filament length, calculated using data from up to 8 individual filaments, are shown in Table 1. The confidence limits given in Table 1 correspond to ± one standard deviation on the mean of

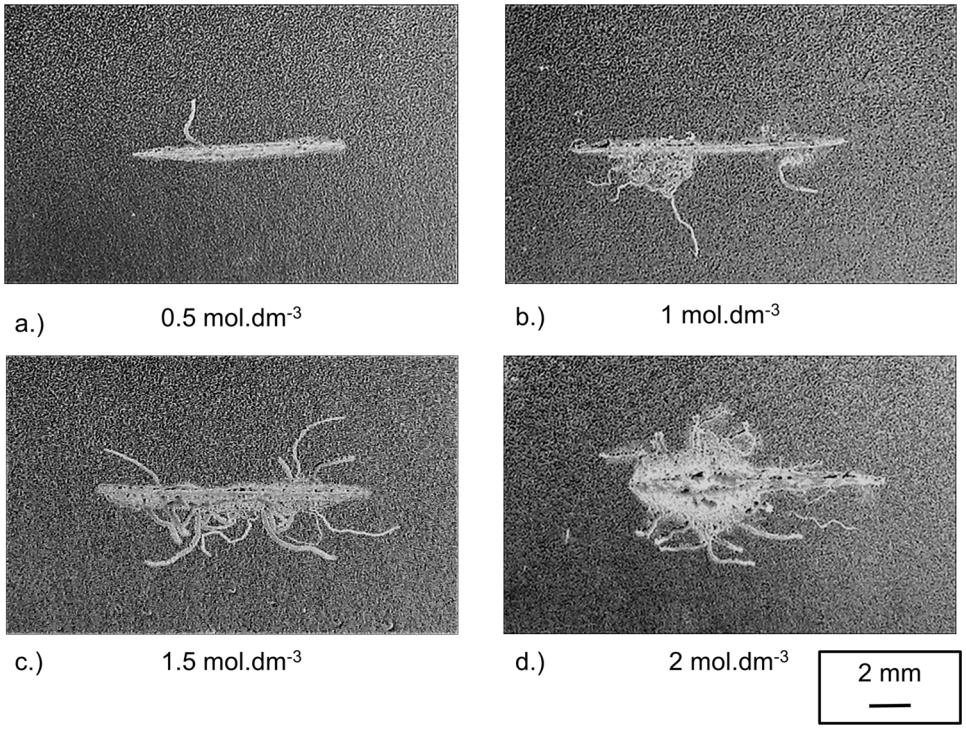

Fig. 8. Optical images of the appearance of ZAM samples 5 weeks after initiation of FFC using varying concentrations of HAc.

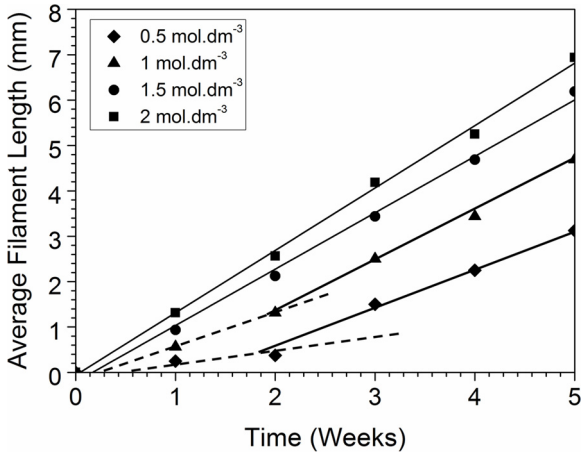

Fig. 9. The time dependent mean filament length for filaments propagating following initiation using each concentration of HAc.

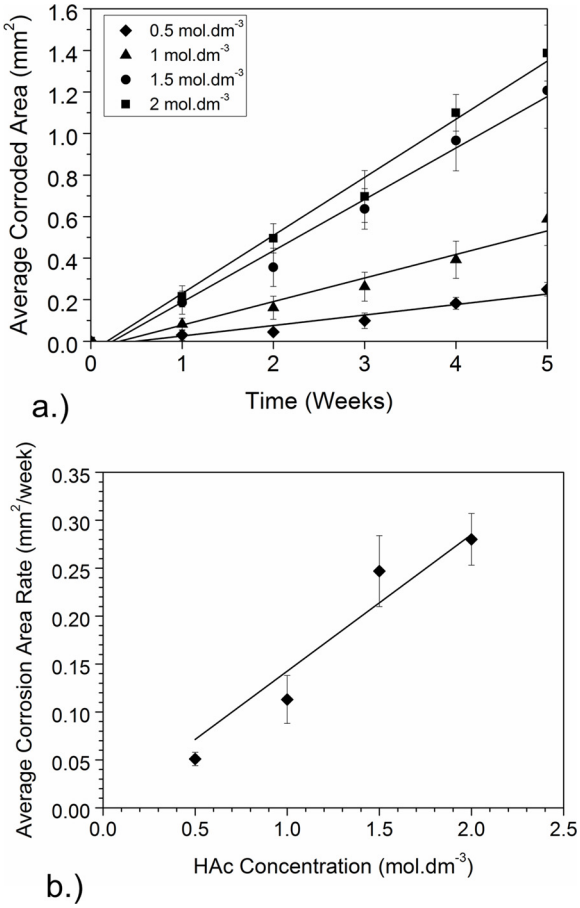

Fig. 10. a.) The time dependent corroded area for the case that FFC is initiated using various concentrations of HAc. The confidence limits (error bars) given correspond to ± one standard deviation on the mean of four measurements and b.) Average corroded area rate as a function of HAc concentration.

eight measurements. The same mean filament length data is plotted vs. time for various initiating concentration of HAc in Fig. 9. For the sake of legibility, the (relatively large) confidence intervals given in Table 1 are not reproduced in Fig. 9. At the lowest HAc concentrations (0.5 mol.dm^{-3} and 1.0 mol.dm^{-3}) there is a concentration dependent initiation period (delay) of 2–4 days. In comparison, for the highest concentration (2 mol.dm^{-3}) initiation occurs almost immediately. It is likely that the initiation time is associated with a corrosion process whereby HAc becomes converted to the solution of metal acetate salts which constitute the filament head electrolyte. Following initiation, the mean filament length increases linearly with time in all cases. The mean filament extension rate for each concentration of HAc was obtained using linear regression (solid lines) and a rate of 0.81 ± 0.04 mm.week^{-1} was obtained for 0.5 mol.dm^{-3} HAc and 1.38 ± 0.04 mm.week^{1} for 2.0 mol.dm^{-3} HAc.

The measurement of filament length is to some extent subjective (because not all filaments are measured) and inevitably gives a large

Table 2
Average FFC corroded area rate, FFC length rate, width of individual filaments and number of filaments per 10 mm artificial scribe defect, for FFC initiated using a range of HAc concentrations.

HAc concentrations (mol. dm^{-3})	dA/dt $mm^2.week^{-1}$	dL/dt $mm.week^{-1}$	Width (mm)	*n*
0.5	0.05 ± 0.01	0.81 ± 0.04	0.16	1
1	0.11 ± 0.03	1.09 ± 0.09	0.10 ± 0.02	4
1.5	0.25 ± 0.04	1.24 ± 0.04	0.18 ± 0.05	16
2	0.28 ± 0.03	1.38 ± 0.04	0.19 ± 0.02	20

scatter (error interval). For these reasons FFC filament area was used as an alternative measure of FFC propagation. The total FFC filament area could be obtained by digital image analysis of the whole filament population following a rapid and objective process. Fig. 10 and Table 2 show total FFC filament area as a function of time for various initiating concentrations of HAc. In all cases total filament area increases linearly with time and straight lines have been constructed through the data using least squares linear regression. The confidence intervals (error bars) shown correspond to ± one standard deviation unit as calculated from four experiments. As in Fig. 9, linear extrapolation gives a non-zero x-axis intercept corresponding to an initiation period (delay). This increases from ~2 days at 2 $mol.dm^{-3}$ HAc to ~4 days at 0.5 $mol.dm^{-3}$ HAc.

The SKP was subsequently used to determine the distribution of Volta potential over actively propagating FFC filaments. Fig. 11a shows an optical image of a PVB coated ZAM sample upon which FFC has developed for approximately 25 weeks. Fig. 11b shows the SKP derived distribution of E_{corr} in the rectangular area indicated in Fig. 11a. Individual filament heads are seen as ~0.2 mm diameter areas of low potential (dark), and the tails as ~0.2 mm wide tracks of high potential (light). These Volta potential distributions are qualitatively similar to those observed in Fig. 3b and distributions previously reported over FFC filaments actively propagating on aluminium alloys [47–51,54], and iron [43–46,53]. Fig. 11c shows the Volta potential measured along axis X-X' in Fig. 11b. Once initiated, individual filaments move away from the coating defect (ie from left right to left). Low potentials of ~-0.55 vs. SHE, consistent with anodic depolarization and dissolution, are observed in the filiform head region. In the tail region the potential values are relatively high at ~-0.2 V vs. SHE, compared to ~-0.32 V vs. SHE in the intact (uncorroded) region. It has previously been shown that the ability of SKP to resolve lateral variations in Volta potential is influenced by the width of the SKP probe electrode and by the probe-sample distance [72]. Consequently, when the features measured (here FFC filaments) exhibit dimensions (here width) similar to the probe-sample distance (100 μm) some instrumental broadening of the measured Volta pattern is to be anticipated. For similar reasons the Volta potential difference measured between discrete features (e.g. FFC head or tail) and a uniform background (e.g. the intact coated surface) will tend to become systematically underestimated [50,53]. This means that the potential contrast in Fig. 11 is likely to be underestimated to some

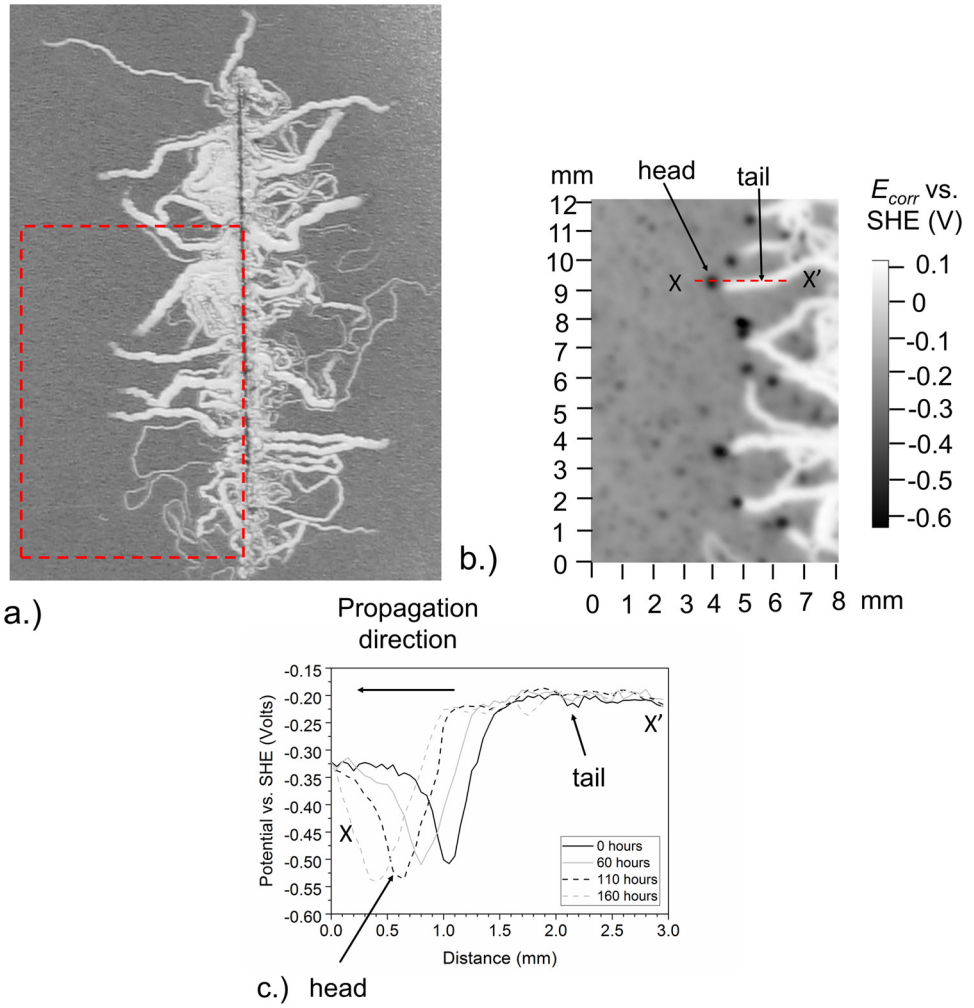

Fig. 11. a.) Optical image of PVB coated ZAM upon which FFC has developed for approximately 25 weeks, b.) SKP derived distribution of E_{corr} in the rectangular area indicated in a.) and c.) E_{corr} values measured along axis X-X'.

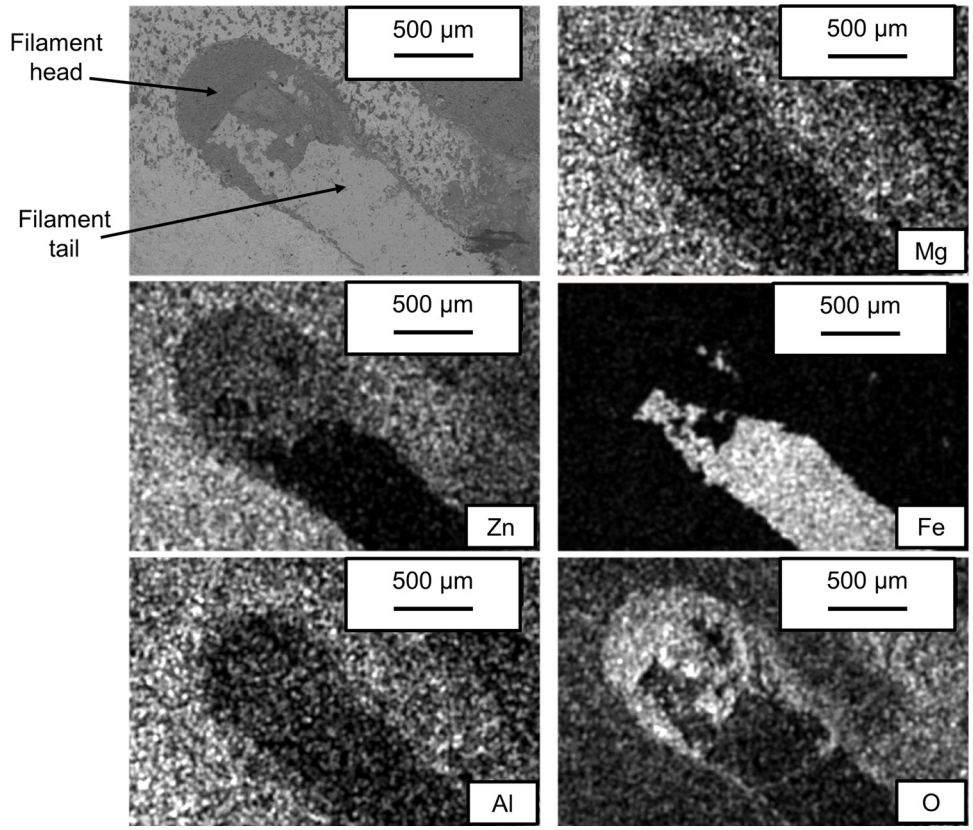

Fig. 12. SEM and EDS elemental maps obtained for a typical FFC head and corrosion product tail which forms on ZAM upon the application of HAc to a PVB coating scribe defect.

extent·

3.4. Post corrosion surface characterisation

Fig. 12 shows SEM and EDS elemental maps obtained for a typical filament which consists of a filament head region and corrosion product tail region. The light areas in each elemental map indicate the presence of the relevant element. During the corrosion of ZAM alloy coatings the predominant corrosion product is expected to be zinc based. The depletion of zinc within the tail region is therefore consistent with some degree of corrosion product removal prior to analysis. The levels of magnesium and aluminium within the tail region are low in relation to the intact coating region whilst iron is only detected within the tail. These findings suggest that the ZAM coating becomes penetrated (as a result of selective phase dissolution) revealing (to some extent) the underlying steel substrate. The increased levels of oxides within the head indicate that the corrosion product was not fully removed during the cleaning process. Fig. 13 shows a backscatter SEM image of an individual FFC filament, and more specifically a FFC head where preferential dissolution of the magnesium-rich eutectic phases has occurred.

The finding that HAc electrolyte selectively attacks magnesium-rich phases within the ZAM microstructure was further investigated by immersing ZAM coated coupons in 0.1 mol.dm^{-3} HAc for up to 5 hours. Samples were removed from the electrolyte hourly and rinsed with distilled water. They were then immersed in hexane for 5 minutes in an ultrasound bath to mechanically remove corrosion products and expose the underlying metal surface. Fig. 14 shows backscatter SEM images of the ZAM surface obtained after various HAc immersion times. The corresponding EDS maps for iron are also shown. The SEM images clearly show the occurrence of selective etching of both the magnesium rich binary and ternary eutectic phases by HAc. This finding is supported by previously published work where initial attack was shown to occur in the $MgZn_2$ phase of both eutectics [18]. After 3 hours of immersion an increase in iron is clearly visible in the EDS maps. After this point the primary zinc dendrites which have, until this point, remained substantially intact, rapidly dissolve leaving a bare steel substrate. This finding is highlighted in Table 3, which shows the wt. % of iron present at various points of time following immersion (as determined using EDS). The quantity of iron on the sample surface increases rapidly from 6 wt. % iron after 4 h to 53 wt. % iron after 5 h.

Cross sections of the coating, obtained after 2 hours of immersion in 0.1 mol.dm^{-3} HAc, were subsequently interrogated using SEM with the aim of determining the extent to which selective phase dissolution occurs at the FFC head. Fig. 15 shows that the binary and ternary eutectic phases have both undergone anodic attack to some extent. Preferential attack of $MgZn_2$ within the binary eutectic is also evident. In comparison the primary zinc dendrites remain substantially intact. It is evident that selective dissolution of magnesium-rich phases has extended through the entire coating thickness and, in places, has reached the iron substrate. It must be recognized that the concentration of free HAc in the FFC filament head electrolyte may be significantly lower than that used here (0.1 mol.dm^{-3}) and the most abundant species is likely to be acetate anion associated with the acetate salts of magnesium, zinc and aluminum. Nevertheless, it seems reasonable to propose that a similar process of magnesium-rich phase dissolution and iron exposure occurs when ZAM is exposed to the filament-head electrolyte droplet.

4. Discussion

4.1. Cathodic delamination and anodic undercutting

The corrosion driven cathodic delamination of organic coatings from the zinc surface of galvanized steel has been widely reported

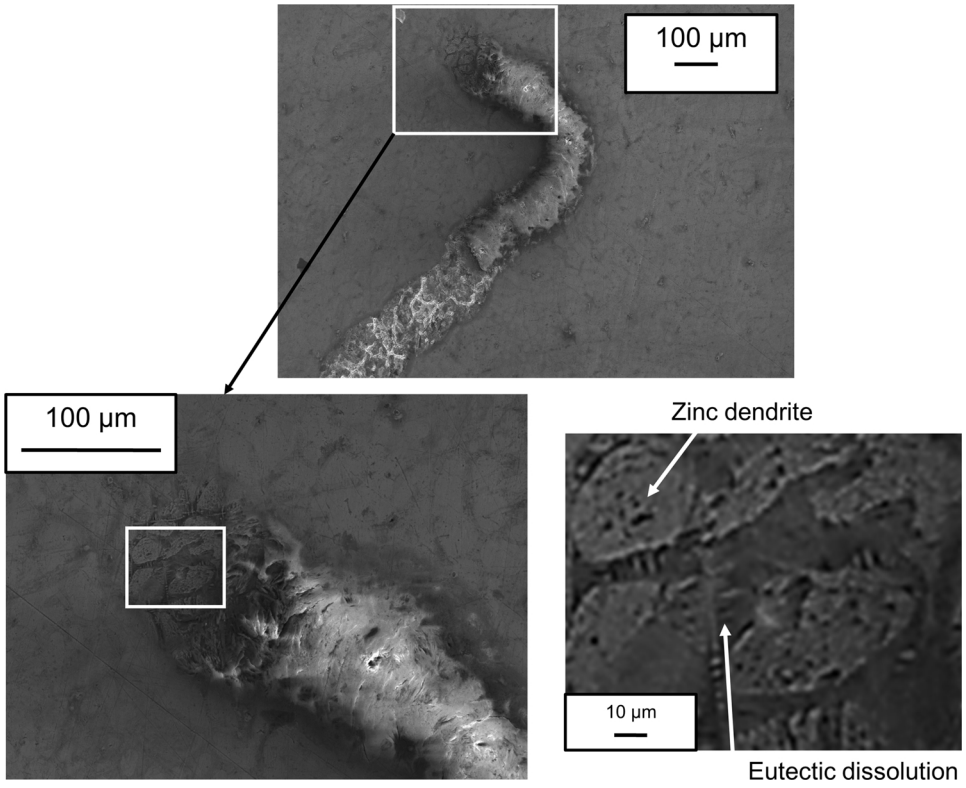

Fig. 13. Backscatter SEM images of an individual filament where dissolution of the eutectic phase within ZAM has occurred.

elsewhere and the kinetics and mechanism of this process are well understood [34–38]. The tendency of the ZAM surface to resist cathodic delamination must therefore be ascribed to the presence of alloying additions (aluminium and/or magnesium). Furthermore, both zinc and zinc-aluminium galvanized coatings have been shown to behave as active cathodes for the ORR [73]. It would therefore seem likely that the failure to observe cathodic delamination from ZAM results not from a general cathodic inactivity of the surface but as a result of the active areas for the ORR (the primary zinc dendrites) being rendered discontinuous by the presence of cathodically in-active magnesium-zinc and magnesium-aluminium-zinc eutectic phases in the coating microstructure. The absence of a continuous cathodic surface would then make advancement of the cathodic delamination front impossible as it could not cross the interpenetrating areas of cathodic inactivity [27].

Previously reported studies on organic coated $MgZn_2$ have similarly shown a high resistance to corrosion driven cathodic delamination [28]. The air-formed surface film on magnesium consists of magnesium oxide and magnesium hydroxide and the band gap values associated with these species are ~7 eV [74] and ~4.25 eV [75], respectively. Both of these values are significantly higher than the band gap for zinc oxide (~3 eV), implying a greater resistance to interfacial electron transfer associated with the ORR [74]. However, it is also known that $MgZn_2$ in contact with corrosive electrolyte undergoes anodic de-alloying by loss of Mg^{2+} and leaves behind a surface enriched in zinc [3]. This zinc rich surface tends to adopt a potential typical for freely corroding zinc (~-0.7 V vs. SHE) [36–39]. The intact (uncorroded) $MgZn_2$ surface exhibits a lower potential (~-1.4 vs. SHE) [28]. It may therefore be understood that no thermodynamic driving force exists for making intact organic-coated $MgZn_2$ a cathode for the ORR when this is galvanically coupled to zinc (or anodically de-alloyed $MgZn_2$) at a coating defect [3]. It has been demonstrated elsewhere that cathodic disbondment can occur from ZAM surfaces when $MgZn_2$ dealloying is inhibited by high defect pH and, on this basis, it has been concluded that the potential effects are more important than surface (hydr)oxide bandgap in preventing cathodic delamination [30].

Whatever the exact mechanism it would seem reasonable to propose that the principal microstructural components conferring resistance to cathodic delamination from the ZAM surface in the present work are the eutectic phases containing $MgZn_2$ lamellae, which exhibit a Volta potential significantly lower (0.2 V) that the primary zinc dendrites (Fig. 2). In comparison, the anodic dissolution and anodic undercutting of the PVB coating observed at the defect/intact coating interface in Fig. 3 are entirely consistent with both the notion of near-defect dealloying and the ability of the ZAM coating to cathodically protect the exposed steel substrate. ZAM coatings have previously been shown to provide a superior resistance to anodic undercutting (anodic edge creep) in comparison with conventional Zn coatings [76,77]. This beneficial effect has been attributed to an improved 'self- healing' effect, induced by the presence of Mg^{2+} ions but is highly dependent upon testing conditions [76,77].

4.2. Susceptibility to FFC

It is evident from Figs. 6–10 that FFC is rapidly and reproducibly initiated on PVB coated ZAM by addition of dilute aqueous HAc to a penetrative organic coating defect. It is also evident from the linearity of the filament extension plots in Fig. 9, and area-time plots in Fig. 10, that the resulting filaments propagate at a substantially constant rate. This finding is typical of FFC in general and is consistent with the notion that acetate (and therefore electrolyte volume) is conserved in the propagating filament head droplet [31,42,43].

Assuming a head droplet electrolyte of approximately constant composition, the volume of electrolyte in isopiestic equilibrium with the relative humidity of the reference solution used in our experiments, will be directly proportional to the number of moles of HAc introduced. Under these circumstances an approximately linear relationship would be expected between FFC area rate and moles of HAc, and this expectation is borne out in Fig. 10b. The observed increase in FFC area propagation rate with increasing moles of HAc initiant (Fig. 10 and Table 2) arises principally from an increase in the number, and width

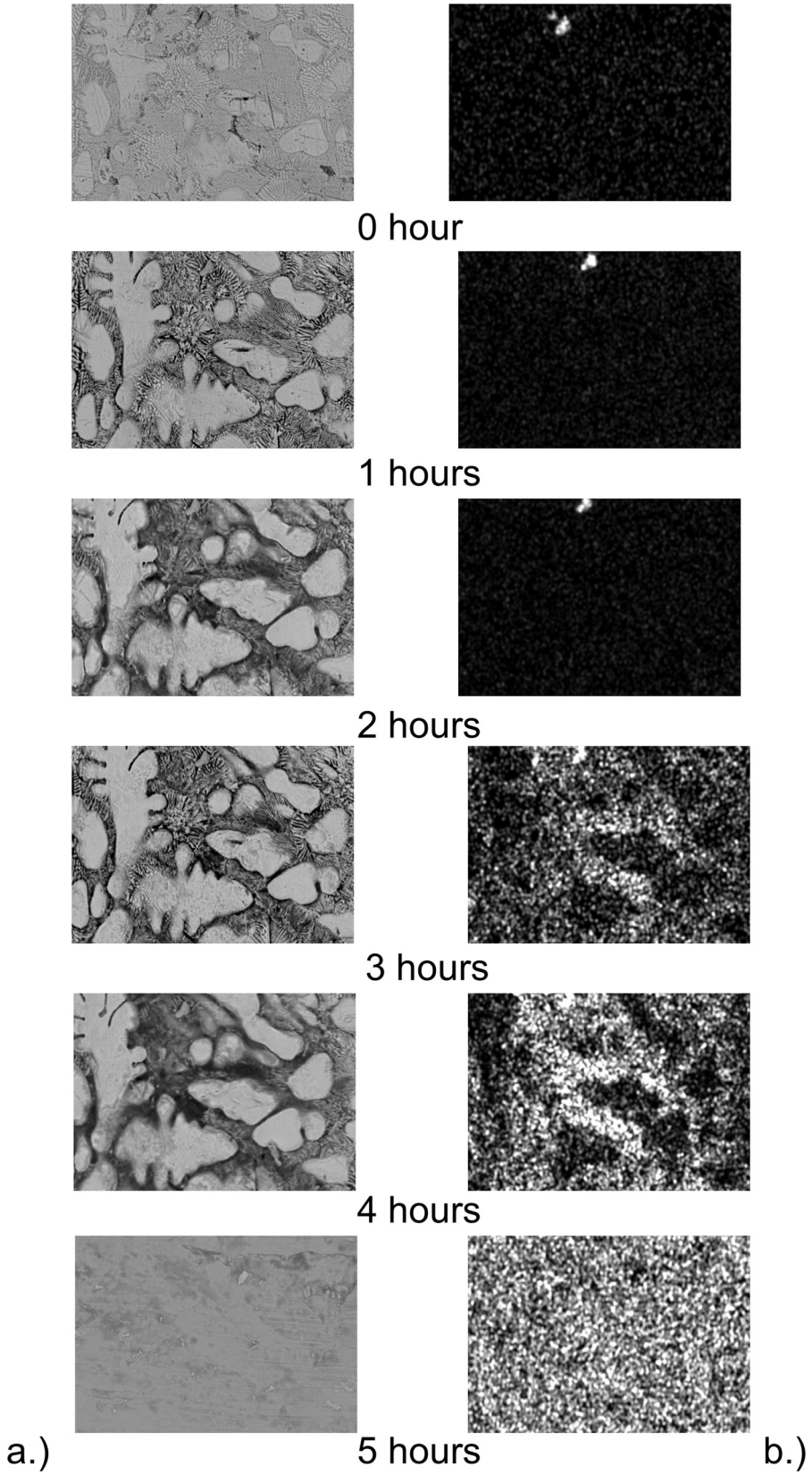

Fig. 14. a.) Backscatter SEM images and b.) corresponding EDS elemental maps of a ZAM surface obtained at after various times of immersion in 0.1 mol.dm^{-3} HAc.

of, FFC filaments. The mean filament length extension rate (Fig. 9 and Table 2) less than doubles for a 4 fold increase in HAc. Furthermore, FFC images such as those in Fig. 6 show no obvious correlation between filament width (head droplet diameter) and filament length extension rate for individual filaments. On the basis of previously published modelling of FFC kinetics, this last finding would suggest a substantial degree of mass transport control in the FFC localized corrosion cell of ZAM. Such mass transport control could arise, for example, ohmically

Table 3
EDS derived wt. % Fe exposed on a ZAM coating at various times following immersion in 0.1 mol.dm^{-3} HAc.

Time (hours)	wt. % Fe
1	0.7
2	0.9
3	4.8
4	6.2
5	53

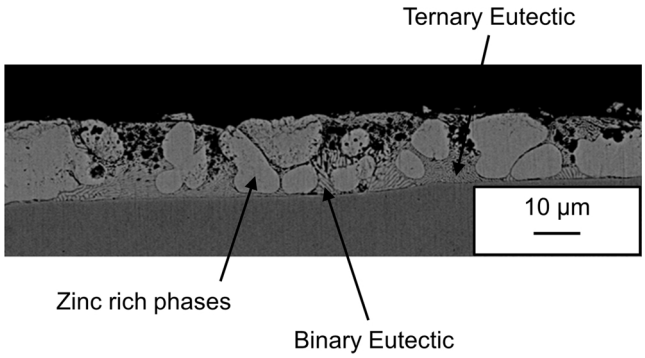

Fig. 15. SEM image of cross sections of the ZAM coating, obtained after 2 hours of immersion in 0.1 mol.dm^{-3} HAc.

as a result of ions migrating through poorly conducting media or along interfaces [50].

The mechanism by which FFC propagates on metals such as aluminium alloys [47–51] and iron [43–46] has been widely reported. It is generally assumed that anodic metal dissolution at the front of the advancing filament droplet is coupled to cathodic O_2 reduction at the back of the droplet [31,42,44–46]. The drive for filament advancement is differential aeration arising from facile O_2 diffusion through the dry, porous corrosion product comprising the filament tail [31,42–44]. To the authors knowledge, FFC has not been reported on Zn galvanised steel. Consequently, the observation, here, of FFC on organically coated ZAM must again be ascribed to the aluminium and/or magnesium alloying additions.

The same authors who reported the high resistance of organically coated $MgZn_2$ to cathodic disbondment pointed out that the low potential of $MgZn_2$ and its tendency to anodically de-alloy, made this material susceptible to coating delamination by anodic undercutting [28]. For these reasons it seems reasonable to propose that the principal component making ZAM susceptible to HAc induced FFC is $MgZn_2$ present in the eutectic phases of the ZAM microstructure. Thus, anodic metal dissolution proceeding (initially at least) through attack on $MgZn_2$ at the front of the filament head droplet (as shown schematically in Fig. 16), could couple with the cathodic ORR on zinc, or iron (exposed through coating dissolution), at the rear of the droplet.

It has been shown elsewhere that the kinetics of anodic attack on $MgZn_2$ can be relatively complex [78]. Either a congruent dissolution of Mg and Zn or a preferential loss of Mg and $MgZn_2$ de-alloying can be observed, depending on the applied potential [78]. Electrolyte composition is also likely to exert an influence. In the current work we are unable to specify the exact mechanism of anodic attack on the ZAM in contact with dilute aqueous HAc and/or the FFC head electrolyte. Neverthelesss, it is evident from Figs. 13–15 that the anodic attack does proceed via a preferential dissolution of Mg-rich phases in the microstructure. One corollary of this finding is that it could reasonably be expected for the propagation of HAc initiated FFC on ZAM to follow a "path of least resistance" and track Mg-rich phases on the ZAM surface. For example, it has been shown elsewhere that FFC filament heads on AA2024 tend to jump from one active intermetallic particle on the alloy

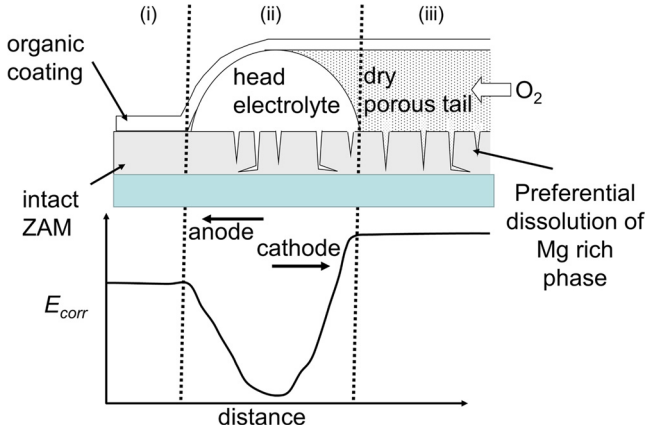

Fig. 16. Schematic showing the proposed mechanism for the propagation of FFC occurring on a ZAM surface and a schematic of the E_{corr} profile measured along the filament axis.

surface to another [79]. In the present work the typical filament head diameter (~200 μm) is up to ten times larger than that of the ZAM microstructural features (15–25 μm) and it is therefore not possible to conclude whether the ZAM microstructure directs filament propagation with any degree of certainty. Nevertheless, this topic is worthy of further investigation.

Such a mechanism for ZAM FFC is immediately consistent with the etched appearance of the ZAM surface in the FFC head region seen in Fig. 13. It is also consistent with the electrochemical potential profile measured along the filament axis using SKP and shown in Fig. 11b, and schematically in Fig. 16. A potential difference of ~0.35 V exists between the filament head and tail, and for the reasons given previously regarding the limited lateral resolution of Kelvin probe measurement, this is probably a conservative estimate. The magnitude and polarity of this potential difference implies a significant driving force for making the FFC tail (or interface between the tail and head droplet) an O_2 cathode in the FFC localized corrosion cell (Fig. 16). Fig. 11 also shows that potentials in the FFC tail region are ~0.15 V higher than those measured over the intact PVB coated ZAM surface. These high tail potentials would be consistent with primary zinc (remaining after magnesium-rich eutectic phases have anodically dissolved) existing in a substantially passive state. However, the same high potentials would be consistent with the partial or complete exposure of substrate iron.

Fig. 12 suggests that iron is actually exposed in the FFC tail and Fig. 13 confirms that selective ZAM phase dissolution, which occurs during immersion in HAc, produces iron exposure in a few hours. The interaction volume associated with EDS means it is not clear whether the Fe observed in Fig. 12 is actively exposed or buried under residual Zn or corrosion product. However, it is clear that the degree to which it is covered has decreased and it is further evident in Fig. 15 that percolating pathways down to the iron substrate would become open long before the ZAM coating was completely removed. Such pathways would allow the iron surface to act as a contributory O_2 cathode and increase the driving force for FFC. Thus, in ZAM, selective phase dissolution and iron exposure may produce a differential cathodic activation which reinforces the effect of differential aeration in FFC. The notion that cathodic drive from iron is important is supported by Fig. 6 which shows that the number and width of FFC filaments is significantly higher in the case that initiation occurs at a scribe defect which penetrates both the PVB and ZAM coating so that the steel substrate is exposed.

Questions then arise as to: 1.) why it is possible to rapidly and reproducibly initiate FFC at a scribed defect on PVB coated ZAM galvanized steel using HAc and not chloride-based electrolytes such as HCl, $FeCl_2$ or NaCl. and 2.) how it was that FFC became initiated (albeit after a very long delay) on a PVB coated ZAM galvanized steel sample where

a large exposed steel defect was in contact with aqueous NaCl. In attempting to answer these questions we would first draw attention to Fig. 4b which shows that (when FFC has been initiated using aqueous NaCl) Cl^- ions become entrapped in the corrosion product constituting the filament tail and are not conserved in the filament head. This finding is in sharp contrast to FFC on PVB coated iron and aluminum, where Cl^- is strongly conserved in the filament head [50,53]. The exact mechanism of Cl^- entrapment remains unclear but it seems reasonable to propose that precipitiation of sparingly soluble zinc hydroxychloride (simonkollite) in the filament tail is responsible. Since the conservation of electrolyte anions is required for ongoing FFC propagation the implication is that Cl^- is likely to be a very inefficient initiant of FFC on ZAM. Sparingly soluble zinc hydroxyacetate salts can similarly form through the alkalization of zinc acetate solutions. However, (unlike simonkollite) these tend to decompose through hydrolysis at room temperature producing zinc hydroxide and releasing acetate [80]. This difference in stability is probably the reason that HAc succeeds as an FFC initiant on ZAM where the chloride based electrolytes fail.

Given the above it seems likely that the FFC seen in Figs. 3 and 4 does not result directly from Cl^- based metal salts constituting a filament head electrolyte but indirectly as a consequence of adventitious HAc production. It is possible that sufficient HAc becomes released through hydrolysis of the PVB coating (actually polyvinyl butyral-co-vinyl alcohol-co-vinyl acetate). However, it should also be recognized that HAc vapour is almost ubiquitous in the indoors environment, being released from wood and through the oxidative degradation of most organic material. At first sight there would appear to be a conflict with the finding in section 3.3 that FFC could not be initiated by injection of NaCl solution into a penetrative coating scribe. However, it should be borne in mind that in section 3.2, a relatively large volume of 0.86 mol.dm^{-3} NaCl solution is in contact with $\sim$1 cm^2 of exposed steel and a similar area of mechanically delaminated PVB for a period of months. In section 3.3, a very small volume of NaCl (2 μL of 2 mol.dm^{-3}) is injected into a narrow penetrative scribe. It seems reasonable to assume that the methodology used in section 3.3 does not result in sufficient acetic acid release for FFC to become initiated over the experimental time period.

When considering the findings presented during this work it should be borne in mind that although HAc induced FFC appears to be a significant mode of organic coating failure on ZAM exposed to an indoor environment, it is likely to be far less common on material exposed to outdoor conditions. Furthermore, ZAM coatings in service are typically phosphated or otherwise pretreated before the application of an organic overcoat and the extent to which such pretreatment mitigates the severity of FFC attack has yet to be determined. Finally, whilst it must be assumed that the solubility and hygroscopicity of the metal acetate salts forming on ZAM are such as to facilitate FFC the exact composition of the filament head electrolyte and the range of RH over which FFC propagation will occur are still unknown.

5. Conclusions

- The PVB overcoated ZAM is susceptible to filiform corrosion (FFC). FFC is rapidly and reproducibly initiated by introduction of small quantities of HAc at a penetrative defect in the PVB overcoat. FFC has been observed following a long exposure to aqueous NaCl at a coating defect where iron is exposed (probably as a result of acetate released through hydrolysis of the PVB coating). However, chloride based electrolytes (NaCl, $FeCl_2$ and HCl) do not reproducibly produce FFC on ZAM.
- Once initiated the FFC delaminated area increases linearly with respect to time. This finding is consistent with acetate being conserved in the FFC filament head droplets. The rate of FFC area increase shows an approximately linear dependence on the quantity (no of moles) of HAc used during initiation.
- There is evidence that preferential anodic dissolution of the magnesium-rich eutectic phases produce pathways in the ZAM coating through which O_2 can diffuse to the iron substrate. Iron exposed in the FFC tail (or tail-head droplet interface) will galvanically couple to ZAM increasing the driving force for filament advance.
- Given that HAc occurs widely in the environment as a product of metabolism, and an intermediate in the environmental degradation of many organic materials (including paints), it seems plausible that the FFC could become a problem on ZAM coated steels.

Acknowledgments

The authors would like to thank Tata Steel for providing samples and EPSRC for the funding for the Engineering Doctorate studentship via the Collaborate Training Account (GR/T11333/01).

References

[1] P. Volovitch, T.N. Vu, C. Allely, A.A. Aal, K. Ogle, Understanding corrosion via corrosion product characterization: II. Role of alloying elements in improving the corrosion resistance of Zn–Al–Mg coatings on steel, Corros. Sci. 53 (2011) 2437–2445, https://doi.org/10.1016/j.corsci.2011.03.016.
[2] X. Zhang, T.N. Vu, P. Volovitch, C. Leygraf, K. Ogle, I. Odnevall Wallinder, The initial release of zinc and aluminium from non-treated Galvalume and the formation of corrosion products in chloride containing media, Appl. Surf. Sci. 258 (2012) 4351–4359, https://doi.org/10.1016/j.apsusc.2011.12.112.
[3] J. Sullivan, N. Cooze, C. Gallagher, T. Lewis, T. Prosek, D. Thierry, In situ monitoring of corrosion mechanisms and phosphate inhibitor surface deposition during corrosion of zinc–magnesium–aluminium (ZMA) alloys using novel time-lapse microscopy, Faraday Discuss. 180 (2015) 361–379, https://doi.org/10.1039/C4FD00251B.
[4] J. Duchoslav, M. Arndt, R. Steinberger, T. Keppert, G. Luckeneder, K.H. Stellnberger, J. Hagler, C.K. Riener, G. Angeli, D. Stifter, Nanoscopic view on the initial stages of corrosion of hot dip galvanized Zn–Mg–Al coatings, Corros. Sci. 83 (2014) 327–334, https://doi.org/10.1016/j.corsci.2014.02.027.
[5] T.N. Vu, P. Volovitch, K. Ogle, The effect of pH on the selective dissolution of Zn and Al from Zn–Al coatings on steel, Corros. Sci. 67 (2013), https://doi.org/10.1016/j.corsci.2012.09.042 42-29.
[6] M. Salgueiro Azevedo, C. Allely, K. Ogle, P. Volovitch, Corrosion mechanisms of Zn (Mg,Al) coated steel: 2. The effect of Mg and Al alloying on the formation and properties of corrosion products in different electrolytes, Corros. Sci. 90 (2015) 482–490, https://doi.org/10.1016/j.corsci.2014.07.042.
[7] T. Prosek, D. Persson, J. Stoulil, D. Thierry, Composition of corrosion products formed on Zn–Mg, Zn–Al and Zn–Al–Mg coatings in model atmospheric conditions, Corros. Sci. 86 (2014) 231–238, https://doi.org/10.1016/j.corsci.2014.05.016.
[8] J.D. Yoo, P. Volovitch, A.A. Aal, C. Allely, K. Ogle, The effect of an artificially synthesized simonkolleite layer on the corrosion of electrogalvanized steel, Corros. Sci. 70 (2013) 1–10, https://doi.org/10.1016/j.corsci.2012.10.024.
[9] P. Volovitch, M. Serdechnova, K. Ogle, Aqueous corrosion of Mg-Al binary alloys: roles of Al and Mg, Corrosion 68 (2012) 557–570, https://doi.org/10.5006/i0010-9312-68-6-557.
[10] T. Lostak, A. Maljusch, B. Klink, S. Krebs, M. Kimpel, J. Flock, S. Schulz, W. Schuhmann, Zr-based conversion layer on Zn-Al-Mg alloy coated steel sheets: insights into the formation mechanism, Electrochim. Acta 137 (2014) 65–74, https://doi.org/10.1016/j.electacta.2014.05.163.
[11] R. Hausbrand, M. Stratmann, M. Rohwerder, Corrosion of zinc–magnesium coatings: mechanism of paint delamination, Corros. Sci. 51 (2009) 2107–2114, https://doi.org/10.1016/j.corsci.2009.05.042.
[12] B. Schuhmacher, C. Schwerdt, U. Seyfert, O. Zimmer, Innovative steel strip coatings by means of PVD in a continuous pilot line: process technology and coating development, Surf. Coat. Technol. 163 (2003) 703–709, https://doi.org/10.1016/S0257-8972(02)00660-6.
[13] J.L. Davies, C.F. Glover, J. Van de Langkruis, E. Zoestbergen, G. Williams, The effect of Mg concentration on the resistance of PVD Zn-Mg coatings to corrosion driven organic coating delamination, Corros. Sci. 100 (2015) 607–618, https://doi.org/10.1016/j.corsci.2015.08.03.
[14] J. Duchoslav, M. Arndt, T. Keppert, G. Luckeneder, D. Stifter, XPS investigation on the surface chemistry of corrosion products on ZnMgAl-coated steel, Anal. Bioanal. Chem. 405 (2013) 7133–7144, https://doi.org/10.1007/s00216-013-7099-3).
[15] S. Schuerz, M. Fleischanderl, G.H. Luckeneder, K. Preis, T. Haunschmied, G. Mori, A.C. Kneissl, Corrosion behaviour of Zn–Al–Mg coated steel sheet in sodium chloride-containing environment, Corros. Sci. 51 (2009) 2355–2363, https://doi.org/10.1016/j.corsci.2009.06.019.
[16] T. Prosek, N. Larche, M. Vlot, F. Goodwin, D. Thierry, Corrosion performance of Zn–Al–Mg coatings in open and confined zones in conditions simulating automotive applications, Mater. Corros. 61 (2010) 412–420, https://doi.org/10.1002/maco.200905425.
[17] L. Jiang, M. Wolpers, P. Volovitch, K. Ogle, Activation and inhibition of Zn–Al and Zn–Al–Mg coatings on steel by nitrate in phosphoric acid solution, Corros. Sci. 60 (2012) 256–264, https://doi.org/10.1016/j.corsci.2012.03.028.

[18] J.H. Sullivan, S. Mehraban, J. Elvins, In situ monitoring of the microstructural corrosion mechanisms of zinc–magnesium–aluminium alloys using time lapse microscopy, Corros. Sci. 53 (2011) 2208–2215, https://doi.org/10.1016/j.corsci.2011.02.043.

[19] J. Elvins, J.A. Spittle, D.A. Worsley, Microstructural changes in zinc aluminium alloy galvanising as a function of processing parameters and their influence on corrosion, Corros. Sci. 47 (2005) 2740–2759, https://doi.org/10.1016/j.corsci.2004.11.011.

[20] J. Elvins, J.A. Spittle, J.H. Sullivan, D.A. Worsley, The effect of magnesium additions on the microstructure and cut edge corrosion resistance of zinc aluminium alloy galvanised steel, Corros. Sci. 50 (2008) 1650–1658, https://doi.org/10.1016/j.corsci.2008.02.005.

[21] T. Prosek, A. Nazarov, U. Bexell, D. Thierry, J. Serak, Corrosion mechanism of model zinc–magnesium alloys in atmospheric conditions, Corros. Sci. 50 (2008) 2216–2231, https://doi.org/10.1016/j.corsci.2008.06.008.

[22] D. Thierry, D. Persson, G. Luckeneder, K.H. Stellnberger, Atmospheric corrosion of ZnAlMg coated steel during long term atmospheric weathering at different worldwide exposure sites, Corros. Sci. 148 (2019) 338–354, https://doi.org/10.1016/j.corsci.2018.12.033.

[23] T. Prosek, J. Hagström, D. Persson, N. Fuertes, F. Lindberg, O. Chocholatý, C. Taxén, J. Šerák, D. Thierry, Effect of the microstructure of Zn-Al and Zn-Al-Mg model alloys on corrosion stability, Corros. Sci. 110 (2016) 71–81, https://doi.org/10.1016/j.corsci.2016.04.022.

[24] E. Diler, S. Rioual, B. Lescop, D. Thierry, B. Rouvellou, Chemistry of corrosion products of Zn and MgZn pure phases under atmospheric conditions, Corros. Sci. 65 (2012) 178–186, https://doi.org/10.1016/j.corsci.2012.08.014.

[25] B. Li, A. Dong, G. Zhu, S. Chu, H. Qian, C. Hu, B. Sun, J. Wang, Investigation of the corrosion behaviors of continuously hot-dip galvanizing Zn-Mg coating, Surf. Coat. Technol. 206 (2012) 3989–3999, https://doi.org/10.1016/j.surfcoat.2012.03.079.

[26] P. Volovitch, C. Allely, K. Ogle, Understanding corrosion via corrosion product characterization: I. Case study of the role of Mg alloying in Zn-Mg coating on steel, Corros. Sci. 51 (2009) 1251–1262, https://doi.org/10.1016/j.corsci.2009.03.005.

[27] N.C. Hosking, M.A. Ström, P.H. Shipway, C.D. Rudd, Corrosion resistance of zinc-magnesium coated steel, Corros. Sci. 49 (2007) 3669–3695, https://doi.org/10.1016/j.corsci.2007.03.032.

[28] R. Hausbrand, M. Stratmann, M. Rohwerder, Delamination resistant zinc alloys: simple concept and results on the system zinc-magnesium, Steel Res. Int. 74 (2003) 453–458, https://doi.org/10.1002/srin.200300212.

[29] R. Hausbrand, M. Stratmann, M. Rohwerder, The physical meaning of electrode potentials at metal surfaces and Polymer/Metal interfaces: consequences for delamination corrosion, passivation, and anodic films, J. Electrochem. Soc. 155 (2008) C369–C379, https://doi.org/10.1149/1.2926589.

[30] A. Vimalanandan, A. Bashir, M. Rohwerder, Zn-Mg and Zn-Mg-Al alloys for improved corrosion protection of steel: some new aspects, Mater. Corros. 65 (2014) 392–400, https://doi.org/10.1002/maco.201307586.

[31] G. Williams, H.N. McMurray, Underfilm/coating corrosion, in: B.R.A. Cottis, M. Graham, R. Lindsay, S. Lyon, T.J.A. Richardson, D.J.D. Scantlebury, H. Stott (Eds.), Shreir'S Corrosion, Elsevier Science, 2009, pp. 988–2004.

[32] A. Leng, H. Streckel, M. Stratmann, The delamination of polymeric coatings from steel. Part 1: calibration of the Kelvinprobe and basic delamination mechanism, Corros. Sci. 41 (1999) 547–578, https://doi.org/10.1016/S0010-938X(98)00166-8.

[33] A. Leng, H. Streckel, M. Stratmann, The delamination of polymeric coatings from steel. Part 2: first stage of delamination, effect of type and concentration of cations on delamination, chemical analysis of the interface, Corros. Sci. 41 (1999) 579–597, https://doi.org/10.1016/S0010-938X(98)00167-X.

[34] G. Williams, H.N. McMurray, Chromate inhibition of corrosion-driven organic coating delamination studied using a scanning kelvin probe technique, J. Electrochem. Soc. 148 (2001) B377–B385, https://doi.org/10.1149/1.1396336.

[35] W. Furbeth, M. Stratmann, Investigation of the delamination of polymer films from galvanized steel with the Scanning Kelvinprobe, Fresenius J. Anal. Chem. 353 (337) (1995) 337–341, https://doi.org/10.1007/BF00322064.

[36] W. Furbeth, M. Stratmann, The delamination of polymeric coatings from electrogalvanised steel – a mechanistic approach.: part 1: delamination from a defect with intact zinc layer, Corros. Sci. 43 (2001) 207–227, https://doi.org/10.1016/S0010-938X(00)00047-0.

[37] W. Furbeth, M. Stratmann, The delamination of polymeric coatings from electrogalvanized steel – a mechanistic approach.: part 2: delamination from a defect down to steel, Corros. Sci. 43 (2001) 229–241, https://doi.org/10.1016/S0010-938X(00)00048-2.

[38] W. Furbeth, M. Stratmann, The delamination of polymeric coatings from electrogalvanized steel – a mechanistic approach.: part 3: delamination kinetics and influence of CO2, Corros. Sci. 43 (2001) 243–254, https://doi.org/10.1016/S0010-938X(00)00049-4.

[39] G. Klimow, N. Fink, G. Grundmeier, Electrochemical studies of the inhibition of the cathodic delamination of organically coated galvanised steel by thin conversion films, Electrochim. Acta 53 (2007) 1290–1299, https://doi.org/10.1016/j.electacta.2007.05.045.

[40] M. Arndt, J. Duchoslav, H. Itani, G. Hesser, C.K. Riener, G. Angeli, K. Preis, D. Stifter, K. Hingerl, Nanoscale analysis of surface oxides on ZnMgAl hot-dip-coated steel sheets, Anal. Bioanal. Chem. 403 (2012) 651–661, https://doi.org/10.1007/s00216-011-5507-0.

[41] C. Commenda, J. Pühringer, Microstructural characterization and quantification of Zn–Al–Mg surface coatings, Mater. Charact. 61 (2010) 943–951, https://doi.org/10.1016/j.matchar.2010.06.008.

[42] A. Bautista, Filiform corrosion in polymer-coated metals, Prog. Org. Coat. 28 (1996) 49–58, https://doi.org/10.1016/0300-9440(95)00555-2.

[43] R.T. Ruggeri, T.R. Beck, An analysis of mass transfer in filiform corrosion, Corrosion-NACE 39 (1983) 452–465, https://doi.org/10.5006/1.3581907.

[44] G. Grundmeier, W. Schmidt, M. Stratmann, Corrosion protection by organic coatings: electrochemical mechanism and novel methods of investigation, Electrochim. Acta 45 (2000) 2515–2533, https://doi.org/10.1016/S0013-4686(00)00348-0.

[45] T.M. Watson, A.J. Coleman, G. Williams, H.N. McMurray, The effect of oxygen partial pressure on the filiform corrosion of organic coated iron, Corros. Sci. 89 (2014) 46–58, https://doi.org/10.1016/j.corsci.2014.08.004.

[46] W.H. Slabaugh, M. Grotheer, Mechanism of filiform corrosion, Ind. Eng. Chem. 46 (1954) 1014–1016, https://doi.org/10.1021/ie50533a053.

[47] W. Schmidt, M. Stratmann, Scanning kelvinprobe investigations of filiform corrosion on aluminum alloy 2024-t3, Corros. Sci. 40 (1998) 1441–1443, https://doi.org/10.1016/S0010-938X(98)00044-4.

[48] J.H.W. de Wit, New knowledge on localized corrosion obtained from local measuring techniques, Electrochim. Acta 46 (2001) 3641–3650, https://doi.org/10.1016/S0013-4686(01)00642-9.

[49] N. LeBozec, D. Persson, D. Thierry, S.B. Axelsen, Effect of climatic parameters on filiform corrosion of coated aluminum alloys, Corrosion 60 (2004) 584–593, https://doi.org/10.5006/1.3287763.

[50] G. Williams, H.N. McMurray, The kinetics of chloride-induced filiform corrosion on aluminum alloy AA2024-T3, J. Electrochem. Soc. 150 (2003) B380–B388, https://doi.org/10.1149/1.1589020.

[51] H.N. McMurray, G. Williams, S. O'Driscoll, Chromate inhibition of filiform corrosion on organic coated AA2024-T3 studied using the scanning kelvin probe, J. Electrochem. Soc. 151 (2004) B406–B414, https://doi.org/10.1149/1.1757460.

[52] G. Williams, R. Grace, Chloride-induced filiform corrosion of organic-coated magnesium, Electrochim. Acta 56 (2011) 1894–1903, https://doi.org/10.1016/j.electacta.2010.09.005.

[53] G. Williams, H.N. McMurray, The mechanism of group (I) chloride initiated filiform corrosion on iron, Electrochem. commun. 5 (2003) 871–877, https://doi.org/10.1016/j.elecom.2003.08.008.

[54] H.N. McMurray, A. Holder, G. Williams, G.M. Scamans, A.J. Coleman, The kinetics and mechanisms of filiform corrosion on aluminium alloy AA6111, Electrochim. Acta 55 (2010) 7843–7852, https://doi.org/10.1016/j.electacta.2010.04.035.

[55] J.V. Kloet, W. Schmidt, A.W. Hassel, M. Stratmann, The role of chromate in filiform corrosion inhibition, Electrochim. Acta 49 (2004) 1675–1685, https://doi.org/10.1016/S0013-4686(03)00256-1.

[56] J.V. Kloet, W. Schmidt, A.W. Hassel, M. Stratmann, The role of chromate in filiform corrosion inhibition, Electrochim. Acta 48 (2003) 1211–1222, https://doi.org/10.1016/S0013-4686(02)00829-0.

[57] C. Leygraf, J. Hedberg, P. Qiu, H. Gil, J. Henriquez, C.M. Johnson, W.R. Whitney, Award lecture: molecular in situ studies of atmospheric corrosion, Corrosion 63 (2007) 715–721, https://doi.org/10.5006/1.3278420.

[58] C.M. Johnson, E. Tyrode, C. Leygraf, Atmospheric corrosion of zinc by organic constituents: I. The role of the Zinc/Water and Water/Air interfaces studied by infrared Reflection/Absorption spectroscopy and vibrational sum frequency spectroscopy, J. Electrochem. Soc. 153 (2006) B113–B120, https://doi.org/10.1149/1.2164788.

[59] C.M. Johnson, C. Leygraf, Atmospheric corrosion of zinc by organic constituents: II. Reaction routes for zinc-acetate formation, J. Electrochem. Soc. 153 (2006) B542–B546, https://doi.org/10.1149/1.2360740.

[60] H. Gil, C. Leygraf, J. Tidblad, GILDES model simulations of the atmospheric corrosion of zinc induced by low concentrations of carboxylic acids, J. Electrochem. Soc. 159 (2012) C123–C128, https://doi.org/10.1149/2.072203jes.

[61] P. Qiu, D. Persson, C. Leygraf, Initial atmospheric corrosion of zinc induced by carboxylic acids: a quantitative in situ study, J. Electrochem. Soc. 156 (2009) C441–C447, https://doi.org/10.1149/1.3240878.

[62] J. Hedberg, S. Baldelli, C. Leygraf, E. Tyrode, Molecular structural information of the atmospheric corrosion of zinc studied by vibrational spectroscopy techniques: I. Experimental approach, J. Electrochem. Soc. 157 (2010) C357–C362, https://doi.org/10.1149/1.3479207.

[63] J. Hedberg, S. Baldelli, C. Leygraf, Molecular structural information of the atmospheric corrosion of zinc studied by vibrational spectroscopy techniques: II. Two and three-dimensional growth of reaction products induced by formic and acetic acid, J. Electrochem. Soc. 157 (2010) C363–C373, https://doi.org/10.1149/1.3479255.

[64] D. Persson, C. Leygraf, Metal carboxylate formation during indoor atmospheric corrosion of Cu, Zn, and Ni, J. Electrochem. Soc. 142 (1995) 1468–1477, https://doi.org/10.1149/1.2048598.

[65] E. Johansson, C. Leygraf, B. Rendahl, Characterisation of corrosivity in indoor atmospheres with different metals and evaluation techniques, Br. Corros. J. 33 (1998) 59–66, https://doi.org/10.1179/000705998798114769.

[66] R.J. Holness, G. Williams, D.A. Worsley, H.N. McMurray, Polyaniline inhibition of corrosion-driven organic coating cathodic delamination on Iron, J. Electrochem. Soc. 152 (2005) B73–B81, https://doi.org/10.1149/1.1850857.

[67] G. Williams, H.N. McMurray, D.A. Worsley, Latent fingerprint detection using a scanning Kelvin microprobe, Journal of Forensic Science 46 (2001) 1085–1092, https://doi.org/10.1520/JFS15103J.

[68] H.O. Jacobs, P. Leuchtmann, O.J. Homan, Resolution and contrast in Kelvin probe force microscopy, J. Appl. Phys. 84 (1998) 1168–1173, https://doi.org/10.1063/1.368181.

[69] S. Hudlet, M. Saint Jean, C. Guthmann, J. Berger, Evaluation of the capacitive force between an atomic force microscopy tip and a metallic surface, Eur. Phys. J. B 2 (1998) 5–10, https://doi.org/10.1007/s100510050219.

[70] S. Belaidi, P. Girard, G. Leveque, Electrostatic forces acting on the tip in atomic force microscopy: modelization and comparison with analytic expressions, J. Appl.

Phys. 81 (1997) 1023–1030, https://doi.org/10.1063/1.363884.
[71] P. Schmutz, G. Frankel, Characterization of AA2024-T3 by scanning kelvin probe force microscopy, J. Electrochem. Soc. 145 (1998) 2285–2295, https://doi.org/10.1149/1.1838633.
[72] H.N. McMurray, G. Williams, Probe diameter and probe-specimen distance dependence in the lateral resolution of a scanning Kelvin probe, J. Appl. Phys. 91 (2002) 1673–1679, https://doi.org/10.1063/1.1430546.
[73] H. Dafydd, D.A. Worsley, H.N. McMurray, The kinetics and mechanism of cathodic oxygen reduction on zinc and zinc–aluminium alloy galvanized coatings, Corros. Sci. 47 (2005) 3006–3018, https://doi.org/10.1016/j.corsci.2005.05.036.
[74] J.-H. Huang, C.-P. Liu, The introduction of magnesium and hydrogen introduction in sputtered zinc oxide thin films, Thin Solid Films 498 (2006) 152–157, https://doi.org/10.1016/j.tsf.2005.07.066.
[75] F. Di Quarto, M.C. Romano, M. Santamaria, S. Piazza, C. Sunseri, A semiempirical correlation between the optical band gap of hydroxides and the electronegativity of their constituents, Russ. J. Electrochem. 36 (2000) 1203–1208, https://doi.org/10.1007/BF02757695.
[76] N. LeBozec, D. Thierry, A. Peltola, L. Luxem, G. Luckeneder, G. Marchiaro, M. Rohwerder, Corrosion performance of Zn–Mg–Al coated steel in accelerated corrosion tests used in the automotive industry and field exposures, Mater. Corros. 64 (2013) 969–978, https://doi.org/10.1002/maco.201206959.
[77] R. Krieg, M. Rohwerder, S. Evers, B. Schuhmacher, J. Schauer-Pass, Cathodic self-healing at cut-edges: the effect of Zn^{2+} and Mg^{2+} ions, Corros. Sci. 65 (2012) 119–127, https://doi.org/10.1016/j.corsci.2012.08.008.
[78] J. Han, K. Ogle, Dealloying of $MgZn_2$Intermetallic in slightly alkaline chloride electrolyte and its significance in corrosion resistance, J. Electrochem. Soc. 164 (2017) C952–C961, https://doi.org/10.1149/2.0341714jes.
[79] C. Senöz, S. Borodin, M. Stratmann, M. Rohwerder, In situ detection of differences in the electrochemical activity of Al2Cu IMPs and investigation of their effect on FFC by scanning Kelvin probe force microscopy, Corros. Sci. 58 (2012) 307–314, https://doi.org/10.1016/j.corsci.2012.02.006.
[80] A.H.M. Leung, S.D. Pike, A.J. Clancy, H. Chun Yau, W. Jun Lee, K.L. Orchard, M.S.P. Shaffer, C.K. Williams, Layered zinc hydroxide monolayers by hydrolysis of organozincs, Chem. Sci. 9 (2018) 2135–2146, https://doi.org/10.1039/C7SC04256F.